

Cite this: *RSC Adv.*, 2015, 5, 70410

Preparation of nano-Ni/meso-Ce–TiO₂ by one-step in a sol–gel system and its catalytic performance for hydrogenolysis of xylitol

Zhiwei Zhou,^a Songshan Dai,^a Juan Qin,^b Pengcheng Yu^a and Wenliang Wu^{*a}

The conventional method for the preparation of metal nanoparticles loaded on a mesoporous metal oxide is tedious, and its chemical and physical properties cannot be optionally controlled. A simple and convenient method by one-step in the AcHE sol–gel system was employed for the preparation of nano-Ni/meso-Ce–TiO₂ samples with different Ni nanoparticle loadings. Their physical and chemical properties were characterized by XRD, liquid N₂ adsorption–desorption, EDX, ICP, FT-IR, H₂-TPR and TEM techniques, and their catalytic performance was investigated in the hydrogenolysis of xylitol. The results show that these samples with ordered mesoporous structures, uniform pore size and large specific surface area can be obtained. The Ni nanoparticles can be well dispersed on the mesoporous Ce–TiO₂ surface. The stability of the Ni nanoparticles on the mesoporous TiO₂ would be promoted by the introduction of a small amount of cerium species. The 8% nano-Ni/meso-Ce–TiO₂ sample shows a higher catalytic performance than other samples. The conversion of xylitol was 87.9% and a total yield of diols of 83.2% can be reached. It shows high stability, and the conversion of xylitol and the total yield of diols decreased slightly after repeating the reaction 8 times. The method provides a valuable reference for the preparation of metal nanoparticles loaded on a mesoporous metal oxide, especially for non-noble metal nanoparticles.

Received 7th May 2015
Accepted 11th August 2015

DOI: 10.1039/c5ra08472e

www.rsc.org/advances

1. Introduction

Metal oxides have been widely applied in catalysis because of their acid–base, electrical conductivity and oxidation–reduction qualities.¹ Compared to traditional metal oxides, mesoporous metal oxides are more suitable as a catalyst carrier owing to their uniform pore system, which can restrain the aggregation of active constituents dispersed on their surface.^{2,3} The mesoporous metal oxides can be successfully templated from nanocrystalline, mesoporous carbon materials, silane-functionalized polymers, organic surfactants and cationic polymers *etc.*^{4–10} The solvent evaporation induced self-assembly process raised by Sanchez *et al.* was regarded as the most effective method for the preparation of mesoporous metal oxides because the inorganic condensation kinetics of non-silicate mesostructures can easily be controlled.^{11,12} According to previous reports, a general sol–gel system, including acetic acid, hydrochloric acid and ethanol, which is denoted as the AcHE system, has been proven to

successfully prepare many multicomponent mesoporous metal oxides.^{13,14}

Metal nanoparticles have attracted extensive attention due to their smaller particle size and larger specific surface area, which are often desired for wide applications in catalysis, electricity, magnetic and optics regions.^{15–18} To improve their catalytic performance, these metal nanoparticles would be dispersed by impregnation or deposition on the carriers including zeolites, mesoporous materials and metal oxides *etc.*^{19–22} Unfortunately, it is hard for the prepared catalysts to work well in practice owing to the aggregation of the pre-synthesized metal nanoparticles. Compared to the catalysts prepared by impregnation or deposition, the pre-synthesized noble metal nanoparticles (Au, Pt and Pd *etc.*) can be dispersed uniformly on the mesoporous metal oxides (SiO₂, ZrO₂, Al₂O₃ and TiO₂ *etc.*) in the AcHE sol–gel system, and the structure of the mesoporous metal oxides would not be affected. Therefore, the method can improve the utilization of noble metal nanoparticles²³ and would provide a new idea for the preparation of nickel based catalysts.

Nickel based catalysts, which were conventionally prepared by impregnation or deposition, are widely used as hydrogenation catalysts because of their low price and high activity. Compared to noble metal nanoparticles, the Ni nanoparticles are difficult to obtain because the precursor is more difficult to restore and they would gather easily. Up to now, the reports

^aChemical Engineering and College of Chemistry and Chemical Engineering, Nanjing Tech University (formerly: Nanjing University of Technology), Nanjing, 210009, P. R. China. E-mail: wwl@njtech.edu.cn

^bTechnology and Finance Service Center of Jiangsu Province, Productivity Center of Jiangsu Province, Nanjing 210042, People's Republic of China. E-mail: qinjuan_1981@163.com

about Ni nanoparticles, whose average particle size is less than 6 nm, are quite few.^{24–26} On the other hand, pre-synthesized Ni nanoparticles would be oxidized and assembled after calcination in the AcHE sol-gel system, and the average particle size of the Ni nanoparticles would not be controlled accurately. Therefore, it is most crucial to develop a method for the preparation of Ni nanoparticles loaded on mesoporous metal oxides without pre-synthesized Ni nanoparticles, and it is still rarely reported so far.

Diols, such as ethylene glycol (EG), 1,2-propylene glycol (1,2-PG) and 1,3-propylene glycol (1,3-PG), are widely used as pharmaceuticals, liquid fuels, antifreeze agents and solvents.²⁷ However, the diols are industrially obtained from petroleum feedstocks by the hydration of ethylene oxide or propylene oxide. The catalytic transformation of polyols to diols has attracted considerable attention.

In this work, the Ni nanoparticles uniformly loaded on the ordered mesoporous Ce-TiO₂ samples prepared by one-step in the AcHE sol-gel system were firstly reported, and the chemical and physical properties were characterized. Their catalytic performances in the hydrogenolysis of xylitol were investigated.

Fig. 1 is the schematic diagram for the preparation of nano-Ni/meso-Ce-TiO₂ samples by one-step. This facile method is based on a sol-gel process combined with the AcHE system using F127 as the template. In the micellar solution of the titanium precursor, the Ni and Ce precursors could be well dispersed, and F127 can cross-link and grow slowly with inorganic precursors in the aging and solvent evaporation processes. After calcination in air and reduction in a hydrogen atmosphere, the Ni and Ce could be directly incorporated into the mesoporous TiO₂. However, the Ni nanoparticles would be adsorbed on the surface of the mesoporous TiO₂ prepared by impregnation, which always results in their aggregation or loss during its application in some reactions.

2. Experimental

2.1. Sample preparation

The mesoporous TiO₂ sample was synthesized according to the literature²³ using F127 as a structure-directing agent and

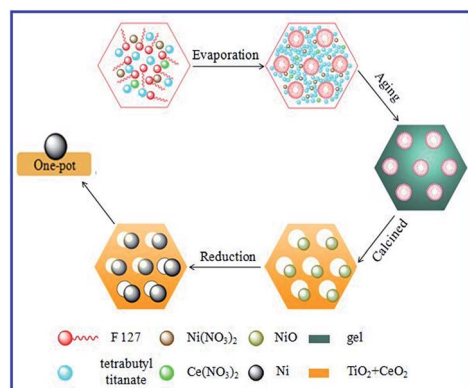


Fig. 1 Schematic diagram for the preparation of the nano-Ni/meso-Ce-TiO₂ sample.

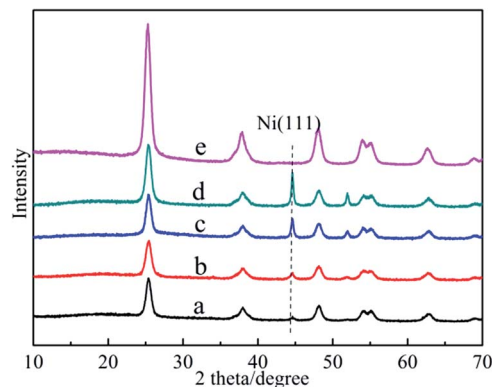


Fig. 2 XRD patterns for the (a) 4% nano-Ni/meso-TiO₂, (b) 8% nano-Ni/meso-TiO₂, (c) 12% nano-Ni/meso-TiO₂, (d) 16% nano-Ni/meso-TiO₂, and (e) meso-TiO₂ samples.

tetrabutyl titanate as the Ti source. In a typical synthesis process, 1.6 g F127, 1.2 g concentrated hydrochloric acid and 2.4 g acetic acid were diluted into 30 ml anhydrous ethanol, and the solution was stirred at 303 K for 10 min to form a transparent solution. After that, 3.4 g tetrabutyl titanate was added into the above solution and stirred for another 2 h at 303 K. The solution was transferred to a Petri dish to evaporate the ethanol at 313 K, and the residual film was aged for 24 h at 338 K. The sample was calcined in air at 623 K for 5 h to remove the organic template and defined as meso-TiO₂.

In order to prepare the nano-Ni/meso-Ce-TiO₂ samples, nickel nitrate (Ni(NO₃)₂·6H₂O) and cerium nitrate

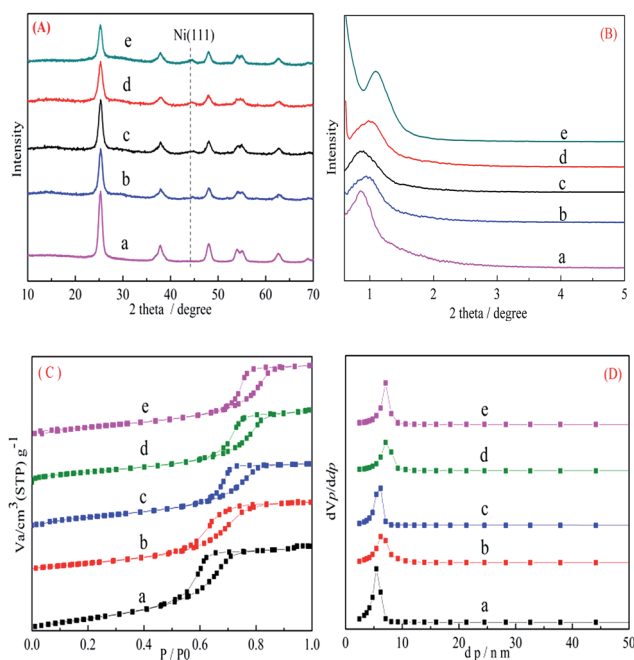


Fig. 3 (A) Wide-angle XRD patterns, (B) low-angle XRD patterns, (C) N₂ adsorption-desorption isotherms and (D) pore size distributions for the (a) meso-Ce-TiO₂, (b) 2% nano-Ni/meso-Ce-TiO₂, (c) 4% nano-Ni/meso-Ce-TiO₂, (d) 6% nano-Ni/meso-Ce-TiO₂, and (e) 8% nano-Ni/meso-Ce-TiO₂ samples.

Table 1 Physical properties for (a) meso-Ce-TiO₂, (b) 2% nano-Ni/meso-Ce-TiO₂, (c) 4% nano-Ni/meso-Ce-TiO₂, (d) 6% nano-Ni/meso-Ce-TiO₂, and (e) 8% nano-Ni/meso-Ce-TiO₂

Samples	D_p (nm)	S_{BET} (m ² g ⁻¹)	V_p (cm ³ g ⁻¹)	Loading (wt%)
a	5.1	214.7	0.30	0.0
b	5.0	180.4	0.28	1.99
c	4.9	155.0	0.26	4.01
d	4.9	147.6	0.25	5.97
e	4.8	137.5	0.23	7.84

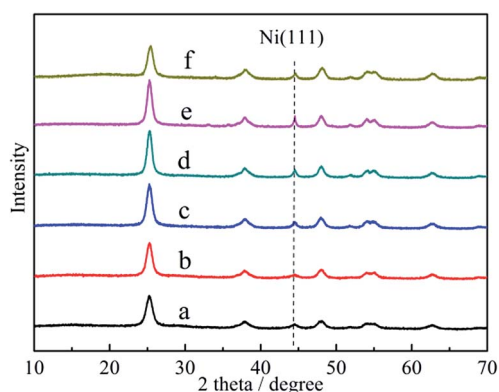


Fig. 4 XRD patterns for 8% nano-Ni/meso-Ce-TiO₂ under different calcination temperatures: (a) 623 K, (b) 673 K, (c) 723 K, (d) 773 K, (e) 823 K and (f) 8% nano-Ni/meso-TiO₂ calcined at 623 K.

Table 2 Physical properties for 8% nano-Ni/meso-Ce-TiO₂ under different calcination temperatures: (a) 623 K, (b) 673 K, (c) 723 K, and (d) 773 K

Samples	D_p (nm)	S_{BET} (m ² g ⁻¹)	V_p (cm ³ g ⁻¹)	D_{Ni} (nm)
a	6.2	126.6	0.23	10.2
b	4.8	137.5	0.23	8.5
c	7.1	123.0	0.22	16.6
d	8.1	105.0	0.20	21.2

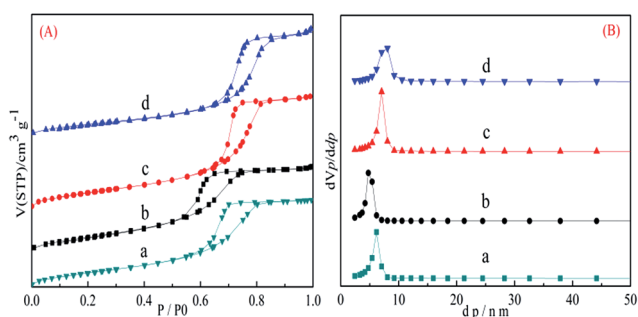


Fig. 5 Liquid N₂ adsorption-desorption isotherms (A) and pore size distribution (B) for 8% nano-Ni/meso-Ce-TiO₂ under different calcination temperatures: (a) 623 K, (b) 673 K, (c) 723 K, and (d) 773 K.

(Ce(NO₃)₂·6H₂O) were used as the Ni and Ce sources, respectively. The nano-Ni/meso-Ce-TiO₂ samples were prepared under the same conditions as the meso-TiO₂, while tetrabutyl titanate

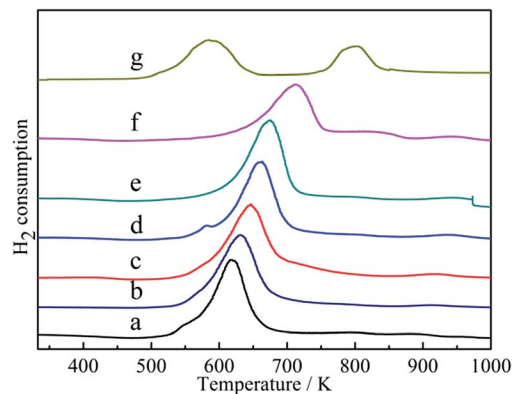


Fig. 6 H₂-TPR profiles for (a) 8% nano-Ni/meso-TiO₂ calcined at 623 K, and 8% nano-Ni/meso-Ce-TiO₂ under different calcination temperatures: (b) 623 K, (c) 673 K, (d) 723 K, (e) 773 K, (f) 823 K and (g) 8% Ni/meso-Ce-TiO₂ (IMP).

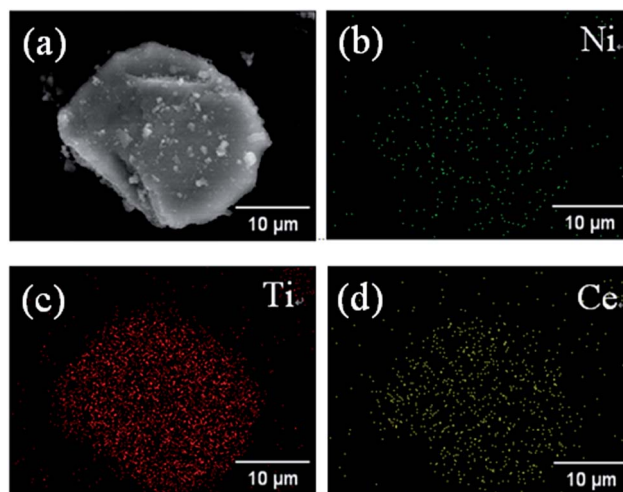


Fig. 7 The SEM photo (a), and electron mapping of particles (b-d), for the 8% nano-Ni/meso-Ce-TiO₂ sample calcined at 673 K.

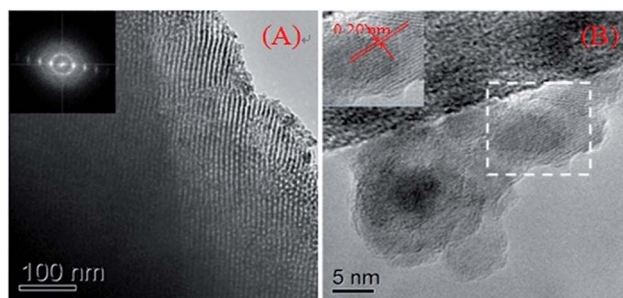


Fig. 8 TEM images for the 8% nano-Ni/meso-Ce-TiO₂ sample calcined at 673 K.

with nickel nitrate and cerium nitrate were added into the solution at the same time. All the samples were reduced under a hydrogen atmosphere at an appropriate temperature except for the samples for H₂-TPR characterization.

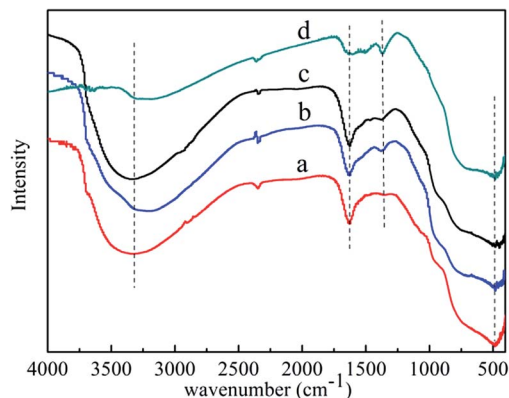


Fig. 9 FT-IR spectra for (a) meso-TiO₂, (b) meso-Ce-TiO₂, (c) 8% nano-Ni/meso-TiO₂, and (d) 8% nano-Ni/meso-Ce-TiO₂.

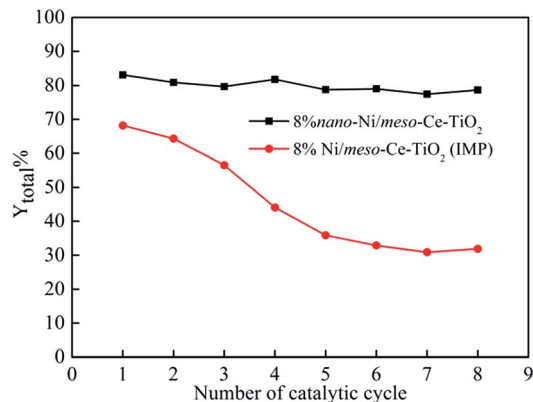


Fig. 10 Catalytic stability for the 8% nano-Ni/meso-Ce-TiO₂ and 8% Ni/meso-Ce-TiO₂ (IMP) catalysts in the hydrogenolysis of xylitol.

For comparison, a sample, defined as 8% Ni/meso-Ce-TiO₂ (IMP), was prepared by the impregnation method.

2.2. Material characterization

2.2.1. X-ray powder diffraction analysis. X-ray powder diffraction patterns of the samples were obtained on a Bruker D8 instrument with Ni-filtered Cu K α radiation ($\lambda = 0.154$ nm) and operated at 40 kV and 30 mA. The scanning rate was 0.05° s⁻¹ in the 2θ range from 0.7° to 5° (low-angle XRD) and from 10° to 70° (wide-angle XRD).

2.2.2. Nitrogen adsorption-desorption analysis. Nitrogen adsorption-desorption isotherms of the samples were measured at 77 K using a Micromeritics Tristar 3000 system. The surface area was calculated using the Brunauer-Emmett-Teller (BET) method in the partial pressure (P/P_0) range from 0.01 to 0.99. The mesoporous size distribution was obtained from the adsorption branch of the isotherm using the Barrett-Joyner-Halenda (BJH) adsorption model.

2.2.3. ICP-OES analysis. The loading of Ni nanoparticles was analyzed by inductively coupled plasma (ICP, Optima2100DV, PerkinElmer, USA) after the sample had been dissolved in HNO₃ solution.

2.2.4. Fourier transform infrared analysis. Fourier transform infrared spectra were obtained on a Thermo Nicolet NEXUS spectrometer with KBr pellets at room temperature.

2.2.5. Temperature-programmed reduction analysis. Temperature-programmed reduction of hydrogen was carried out in a quartz U-tube reactor, and 300 mg sample was used for

each measurement. The sample was pretreated in the argon stream at 623 K for 3 h and then cooled down to room temperature. After that, the mixture of argon and hydrogen was introduced. The temperature was raised from 313 K to 1073 K at a rate of 5 K min⁻¹. The consumption of H₂ in the reactant stream was recorded by a thermal conductivity detector (TCD).

2.2.6. TEM measurement. The morphology of the samples was visualized using a JEOL JEM 2100 transmission electron microscope (TEM) operated at 120 kV. The samples were dispersed in ethanol assisted by an ultrasonic technique.

2.2.7. EDX measurement. The dispersion of the semi-quantitative elemental composition (Ti, Ce, Ni) was verified by energy dispersive X-ray (EDX) spectrometer analysis in the Oxford INCA EDAX Detecting Unit.

2.3. Catalytic reaction

The catalytic hydrogenolysis of xylitol was carried out in a 100 ml stainless steel autoclave equipped with a magnetically driven impeller. 0.5 g catalyst was added into the solution of 7.5 g xylitol and 50 ml deionized water. The reactor was flushed multiple times with hydrogen to replace air. The reaction was carried out at 513 K and 5 MPa for 4 h at a stirring speed of 1000 rpm. At completion of the reaction, the reactor was cooled down to room temperature and the products were collected. The xylitol was analyzed using HPLC equipped with a Hyper REZ XP carbohydrate Ca²⁺ 8 μ m column and an ERC RefractoMax 520 detector. The diols were analyzed on a SP-6890 gas chromatograph equipped with a SE-30 column (0.25 μ m \times 50 m) and a

Table 3 Catalytic performance of different catalysts in the hydrogenolysis of xylitol

Catalysts	Conversion (%)	Yield (%)			Y _{total} (%)
		EG	1,2-PG	1,3-PG	
2% nano-Ni/meso-Ce-TiO ₂	42.1	21.8	6.1	2.8	30.7
4% nano-Ni/meso-Ce-TiO ₂	61.3	34.7	10.9	6.5	52.1
6% nano-Ni/meso-Ce-TiO ₂	77.3	45.5	11.8	12.9	70.2
8% nano-Ni/meso-Ce-TiO ₂	87.9	50.2	17.0	16.0	83.2
8% Ni/meso-Ce-TiO ₂ (IMP)	74.5	41.4	14.9	11.9	68.2

flame ionization detector. The catalytic stability was investigated by filtration without any treatment in the next run.

3. Results and discussion

3.1. Sample characterization

Fig. 2 shows the XRD patterns of the meso-TiO₂ and nano-Ni/meso-TiO₂ samples with different Ni nanoparticle loadings. From Fig. 2, it can be seen that the meso-TiO₂ sample shows a typical anatase tetragonal crystal structure and its crystallite size is about 7.5 nm calculated by the Scherrer equation,²⁸ which is much smaller than that of commercial TiO₂ samples. For different nano-Ni/meso-TiO₂ samples, the characteristic diffraction peak corresponding to the Ni (111) phases²⁹ is present in the all samples, whose intensity increases with the increasing Ni nanoparticle loading. For the 8% nano-Ni/meso-TiO₂ sample, the crystallite size of the TiO₂ and Ni nanoparticles is about 8.5 nm and 19.4 nm calculated by the Scherrer equation, respectively.

In order to reduce the crystallite size of the Ni nanoparticles, a cerium species was introduced into the nano-Ni/meso-TiO₂ samples.^{30,31} XRD patterns, N₂ adsorption-desorption and pore size distributions of the meso-Ce-TiO₂ and nano-Ni/meso-Ce-TiO₂ samples are shown in Fig. 3. Compared to the 8% nano-Ni/meso-TiO₂ sample, it can be seen from Fig. 3(A) that the characteristic diffraction peak corresponding to the Ni (111) phases for the 8% nano-Ni/meso-Ce-TiO₂ sample became wider and could be ignored owing to the smaller crystallite size of the Ni nanoparticles, which is about 8.5 nm calculated by the Scherrer equation. A strong peak around 1° from Fig. 3(B) and typical type-IV N₂ adsorption-desorption isotherms from Fig. 3(C) can be observed for all the samples, suggesting they have a hexagonal ordered mesoporous structure.²⁹ With the increasing Ni nanoparticle loading, the peak would be shifted to a higher degree, which indicates that the interplanar spacing decreased on the basis of the Bragg equation.³² The physical properties for all the samples are listed in Table 1. It can be seen that the samples have a large specific surface area, pore volume and pore size, which are beneficial to its catalytic performance, although there is a decrease with the increase of the Ni nanoparticle loading.

The calcination temperature would affect severely the interaction of the components of the samples.³³ The influence of calcination temperature on the structure of 8% nano-Ni/meso-Ce-TiO₂ was studied, and the XRD patterns are shown in Fig. 4. When the calcination temperature increased up to 723 K, the diffraction peak corresponding to Ni (111) can be obviously observed, and the peak intensity would be promoted with the calcination temperature increasing, which indicates that some bulk aggregates of the Ni species were formed. The average crystallite size of the Ni nanoparticles calculated by the Scherrer equation is listed in Table 2. When the calcination temperature was 673 K, the average crystallite size of the Ni nanoparticles was smaller than that of the others, which was about 8.5 nm. Although the calcination temperatures are the same, compared to sample f, the characteristic diffraction peak corresponding to Ni (111) for sample a is broader, which can conclude that the

crystallite size of the Ni nanoparticles would be reduced by the introduction of a small amount of cerium species.

The liquid N₂ adsorption-desorption isotherms and the pore size distribution for the 8% nano-Ni/meso-Ce-TiO₂ sample under different calcination temperatures are shown in Fig. 5, and the physical properties are listed in Table 2. All the samples can keep their mesoporous character well, and their pore size is uniform. From Table 2, a pore size from 6.2 nm to 4.8 nm and a specific surface area from 126.6 m² g⁻¹ to 137.5 m² g⁻¹ can be obtained when the calcination temperature increases from 623 K to 673 K, which may be due to the stronger interaction between the Ni nanoparticles and the meso-Ce-TiO₂ carrier resulting in the increase of the Ni nanoparticle dispersity.³³ However, with a further increase of the calcination temperature, the surface area decreased, which would be attributed to the sintering of TiO₂ probably.³⁴ Therefore, the appropriate calcination temperature for the 8% nano-Ni/meso-Ce-TiO₂ sample is 673 K.

In order to understand the nature of the Ni nanoparticles clearly, the H₂-TPR, SEM, TEM and FT-IR techniques were utilized. The H₂-TPR profiles of different samples are shown in Fig. 6. One major peak between 627 K and 716 K was observed for samples a-f prepared by the one-pot method, which was assigned to the reduction of NiO interacting with the carrier.^{35,36} Compared to sample a, the peak for sample b was shifted to a higher temperature because of the stronger interaction, which implied that the introduction of a small amount of cerium species can increase the dispersion of the Ni nanoparticles.³⁷ At the same time, the interaction was strengthened with the calcination temperature increased. Two major peaks, one at 553 K and another at 818 K, were observed for sample g prepared by the impregnation method, which is due to the reduction of bulk NiO and NiO interacting with the carrier, respectively. It can be concluded that the Ni nanoparticles are not uniformly dispersed by the impregnation method.³⁸

The SEM photos and election mapping of particles for the 8% nano-Ni/meso-Ce-TiO₂ sample are shown in Fig. 7. As displayed in Fig. 7(a), a granular morphology was obtained. It can be seen from Fig. 7(b-d) that the EDX element mapping showed uniform X-ray intensities of the Ni and Ce signals, suggesting a homogeneous distribution of the Ni nanoparticles in the meso-Ce-TiO₂ matrix,³⁹ which agrees with the XRD analysis.

Fig. 8 shows the TEM images for the 8% nano-Ni/meso-Ce-TiO₂ sample calcined at 673 K. From Fig. 8(A), the typical ordered mesostructure was obviously observed, which was in good agreement with the intense XRD peak at a low-angle. Additional proof for the crystallinity analysis of the framework walls is given by the high-resolution TEM image (Fig. 8(B)).

The (111) planes can be identified by the typical interfringe distance of 0.20 nm, which is close to the lattice spacing of the (111) planes of the face-centered cubic Ni crystal (0.203 nm). It reveals that several crystalline Ni nanoparticles with well-defined lattice planes exist.^{40,41}

FT-IR spectra of different samples are shown in Fig. 9. The bands between 400 and 900 cm⁻¹ could be assigned to the stretching vibration of the Ti-O bond.⁴² Compared to sample a, a new band at about 1300 cm⁻¹, which is attributed to the

emergence of Ti–O–M (M = metal ions), is observed for the other three samples when the cerium or nickel species is introduced. It can be concluded that the cerium or nickel species can be inserted into the framework of the mesoporous TiO₂ sample.^{42–45}

3.2. Catalytic performance of different catalysts for the hydrogenolysis of xylitol

The catalytic performances of different catalysts in the hydrogenolysis of xylitol are listed in Table 3. From Table 3, it can be seen that with the Ni nanoparticle loading increasing from 2% to 8%, the conversion of xylitol increased. The most active catalyst was 8% nano-Ni/meso-Ce–TiO₂, giving a xylitol conversion of 87.9% and a diol total yield of 83.2%. However, although the Ni species loading is the same, the catalytic performance of the 8% nano-Ni/meso-Ce–TiO₂ sample prepared by the one-pot method is much higher than that of the 8% Ni/meso-Ce–TiO₂ (IMP) sample prepared by the impregnation method, which shows a xylitol conversion of 74.5% and a diol total yield of 68.2%, respectively. The results demonstrated the superior ability of the one-pot method for dispersing/incorporating Ni nanoparticles into mesoporous TiO₂.

The catalytic stability of the 8% nano-Ni/meso-Ce–TiO₂ and 8% Ni/meso-Ce–TiO₂ (IMP) catalysts in the hydrogenolysis of xylitol was investigated, and the results are shown in Fig. 10. It can be seen that the total yield of diols decreased slightly, and it can reach about 78.7% after repeating the reaction 8 times, which suggested that the catalytic stability is kept well. However, the total yield of diols decreased severely, and it is only 31.9% after repeating the reaction 8 times for 8% Ni/meso-Ce–TiO₂ (IMP), which may be due to the loss of the Ni species.

4. Conclusions

Ni nanoparticles well-dispersed on meso-Ce–TiO₂ by one-step in the AChE sol–gel system have been developed in this article and investigated in the hydrogenolysis of xylitol. Characterization results revealed that the prepared samples possessed an ordered mesoporous character. Meanwhile, a small amount of cerium species introduced into the meso-TiO₂ can increase the stability of the Ni nanoparticles and reduce the crystallite size of the Ni nanoparticles. The catalytic performance of 8% nano-Ni/meso-Ce–TiO₂ was much higher than that of 8% Ni/meso-Ce–TiO₂ (IMP) although their Ni species loading is the same. The catalytic stability for 8% nano-Ni/meso-Ce–TiO₂ is kept well, and the total yield of diols is 78.7% after repeating the reaction 8 times. The method can provide a guide for the preparation of non-noble metal catalysts with high catalytic performance and give these samples a good application prospect.

Acknowledgements

This work was supported by Jiangsu Planned Projects for Post-doctoral Research Funds (1302121C); Open Project of Beijing Key Laboratory for Enze Biomass and Fine Chemicals; Project

Funded by the Priority Academic Program Development of Jiangsu Higher Education Institutions.

Notes and references

- 1 Y. Ren, Z. Ma and P. G. Bruce, *Chem. Soc. Rev.*, 2012, **41**, 4909–4927.
- 2 R. Y. Zhang, A. A. Elzatahry, S. S. Al-Deyab and D. Y. Zhao, *Nano Today*, 2012, **7**, 344–366.
- 3 A. Corma, *Chem. Rev.*, 1997, **97**, 2373–2419.
- 4 J. S. Beck, J. C. Vartuli, W. J. Roth, M. E. Leonowicz, C. T. Kresge, K. D. Schmitt, C. T. W. Chu, D. H. Olson, E. W. Sheppard, S. B. McCullen, J. B. Higgins and J. L. Schlenker, *J. Am. Chem. Soc.*, 1992, **114**, 10834–10843.
- 5 C. T. Kresge, M. E. Leonowicz, W. J. Roth, J. C. Vartuli and J. S. Beck, *Nature*, 1992, **359**, 710–712.
- 6 A. Firouzi, D. Kumar, L. M. Bull, T. Besier, P. Sieger, Q. Huo, S. A. Walker, J. A. Zasadzinski, C. Glinka, J. Nicol, D. Margolese, G. D. Stucky and B. F. Chmelka, *Science*, 1995, **267**, 1138–1143.
- 7 F. Jiao and P. G. Bruce, *Angew. Chem., Int. Ed.*, 2004, **43**, 5958–5961.
- 8 J. Roggenbuck and M. Tiemann, *J. Am. Chem. Soc.*, 2005, **127**, 1096–1097.
- 9 M. Kang, D. Kim, S. H. Yi, J. U. Han, J. E. Yie and J. M. Kim, *Catal. Today*, 2004, **93**, 695–699.
- 10 S. Polarz, A. V. Orlov, F. Schuth and A. H. Lu, *Chem.–Eur. J.*, 2007, **13**, 592–597.
- 11 C. J. Brinker, Y. F. Lu, A. Sellinger and H. Y. Fan, *Adv. Mater.*, 1999, **11**, 579–585.
- 12 D. Grosso, F. Cagnol, G. Soler-Illia, E. L. Crepaldi, H. Amenitsch, A. Brunet-Bruneau, A. Bourgeois and C. Sanchez, *Adv. Funct. Mater.*, 2004, **14**, 309–322.
- 13 J. Fan, S. W. Boettcher and G. D. Stucky, *Chem. Mater.*, 2006, **18**, 6391–6396.
- 14 Y. H. Dai, X. Q. Yan, Y. Tang, X. N. Liu, L. P. Xiao and J. Fan, *ChemCatChem*, 2012, **4**, 1603–1610.
- 15 B. H. Kim, M. J. Hackett, J. Park and T. Hyeon, *Chem. Mater.*, 2014, **26**, 59–71.
- 16 L. H. Reddy, J. L. Arias, J. Nicolas and P. Couvreur, *Chem. Rev.*, 2012, **112**, 5818–5878.
- 17 P. Claus, A. Bruckner, C. Mohr and H. Hofmeister, *J. Am. Chem. Soc.*, 2000, **122**, 11430–11439.
- 18 S. Carencio, Y. Hu, I. Florea, O. Ersen, C. Boissiere, N. Mezailles and C. Sanchez, *Chem. Mater.*, 2012, **24**, 4134–4145.
- 19 C. H. Christensen, K. Johannsen and I. Schmidt, *J. Am. Chem. Soc.*, 2003, **125**, 13370–13371.
- 20 Y. J. Han, J. M. Kim and G. D. Stucky, *Chem. Mater.*, 2000, **12**, 2068–2069.
- 21 M. Wang, F. Wang, J. P. Ma, C. Chen, S. Shi and J. Xu, *Chem. Commun.*, 2013, **49**, 6623–6625.
- 22 M. Wang, F. Wang, J. P. Ma, M. Li, Z. Zhang, Y. H. Wang, X. C. Zhang and J. Xu, *Chem. Commun.*, 2014, **50**, 292–294.
- 23 J. J. Liu, S. H. Zou, S. Li, X. F. Liao, Y. J. Hong, L. P. Xiao and J. Fan, *J. Mater. Chem. A*, 2013, **1**, 4038–4047.

- 24 S. Tomiyama, R. Takahashi, S. Sato, T. Sodsawa and S. Yoshida, *Appl. Catal., A*, 2003, **241**, 349–361.
- 25 S. Alkhalidi and M. M. Husein, *Energy Fuels*, 2014, **28**, 643–649.
- 26 M. F. Calderon, E. Zelaya, G. A. Benitez, P. L. Schilardi, A. H. Creus, A. G. Orive, R. C. Salvarezza and F. J. Ibanez, *Langmuir*, 2013, **29**, 4670–4678.
- 27 A. M. Ruppert, K. Weinberg and R. Palkovits, *Angew. Chem., Int. Ed.*, 2012, **51**, 2564–2601.
- 28 Y. H. Dai, X. Q. Yan, Y. Tang, X. N. Liu, L. P. Xiao and J. Fan, *ChemCatChem*, 2012, **4**, 1603–1610.
- 29 L. L. Xu, H. L. Song and L. J. Chou, *ACS Catal.*, 2012, **2**, 1331–1342.
- 30 D. Andreeva, I. Ivanova, L. Ilieva and M. V. Abrashev, *Appl. Catal., A*, 2006, **302**, 127–132.
- 31 C. Daza, A. Kiennemann, S. Moreno and R. Molina, *Energy Fuels*, 2009, **23**, 3497–3509.
- 32 Y. F. Zhu, X. Kong, X. Q. Li, G. Q. Ding, Y. L. Zhu and Y. W. Li, *ACS Catal.*, 2014, **4**, 3612–3620.
- 33 S. Badoga, R. V. Sharma, A. K. Dalai and J. Adjaye, *Ind. Eng. Chem. Res.*, 2014, **53**, 18729–18739.
- 34 N. Yao, J. X. Chen, J. X. Zhang and J. Y. Zhang, *Catal. Commun.*, 2008, **9**, 1510–1516.
- 35 J. X. Chen, N. Yao, R. J. Wang and J. Y. Zhang, *Chem. Eng. J.*, 2009, **148**, 164–172.
- 36 M. J. Lazaro, Y. Echevoyen, C. Alegre, I. Suelves, R. Moliner and J. M. Palacios, *Int. J. Hydrogen Energy*, 2008, **33**, 3320–3329.
- 37 F. H. Meng, Z. Li, J. Liu, X. X. Cui and H. Y. Zheng, *J. Nat. Gas Sci. Eng.*, 2015, **23**, 250–258.
- 38 K. Wang, X. J. Li, S. F. Ji, X. J. Shi and J. J. Tang, *Energy Fuels*, 2009, **23**, 25–31.
- 39 J. J. Liu, X. P. Wu, S. H. Zou, Y. H. Dai, L. P. Xiao, X. Q. Gong and J. Fan, *J. Phys. Chem. C*, 2014, **118**, 24950–24958.
- 40 P. Li, J. Y. Liu, N. Nag and P. A. Croziers, *J. Phys. Chem. B*, 2005, **109**, 13883–13890.
- 41 O. Metin, V. Mazumder, S. Ozkar and S. S. Sun, *J. Am. Chem. Soc.*, 2010, **132**, 1468–1469.
- 42 Y. Xu, J. Q. Ma, Y. F. Xu, H. Li, H. X. Li, P. Li and X. G. Zhou, *Appl. Catal., A*, 2012, **413**, 350–357.
- 43 C. Daza, A. Kiennemann, S. Moreno and R. Molina, *Energy Fuels*, 2009, **23**, 3497–3509.
- 44 P. Li, Y. Xin, Q. Li, Z. P. Wang, Z. L. Zhang and L. R. Zheng, *Environ. Sci. Technol.*, 2012, **46**, 9600–9605.
- 45 Y. X. Zhang, G. H. Li, Y. C. Wu, Y. Y. Luo and L. D. Zhang, *J. Phys. Chem. B*, 2005, **109**, 5478–5481.